IEEE Access
Multidisciplinary | Rapid Review | Open Access Journal

Received August 26, 2019, accepted September 20, 2019, date of publication September 24, 2019, date of current version October 7, 2019.

Digital Object Identifier 10.1109/ACCESS.2019.2943398

Modeling and Control of Inverter Zero-Voltage-Switching for Inductive Power Transfer System

JIANGTAO LIU[1,2], QIJUN DENG[1], WENBIN WANG[3], AND ZHIFAN LI[1]

[1]School of Electrical Engineering and Automation, Wuhan University, Wuhan 430072, China
[2]School of Physical, Mechanical, and Electrical Engineering, Hubei University of Education, Wuhan 430205, China
[3]Electric Power Research Institute, State Grid Jiangxi Electric Power Company Ltd., Nanchang 330096, China

Corresponding authors: Qijun Deng (dqj@whu.edu.cn) and Zhifan Li (756502935@qq.com)

This work was supported in part by the National Natural Science Foundation of China under Grant 51907054 and Grant 51677139, and in part by the Hubei Natural Science Foundation under Grant 2017CFB402.

ABSTRACT It's very important to maintain the inverter zero-voltage-switching(ZVS) for inductive power transfer (IPT) system, especially for those high power applications. The ZVS condition can be obtained via regulating the inverter operating frequency of the IPT system. A modeling method based on the energy-amplitude and phase is proposed and corresponding controller is designed to maintain the inverter ZVS condition for IPT. The dynamic model of the ZVS for the half-bridge inverter is developed firstly. To facilitate the dynamic performance analysis and controller design, the original time-variant model is linearized with small-signal method at its operating point, which yields to a 4 order transfer function model. A PI controller which maintains ZVS condition via regulating the inverter operating frequency is designed based on the transfer function. An IPT prototype is built to verify the proposed theory. Experiments show that the controller traces the reference of the ZVS angle within 20 ms under various perturbation, which verifies the correction and effectiveness of the model and controller.

INDEX TERMS Inductive power transfer, PI controller, small-signal modeling, zero-voltage-switching.

I. INTRODUCTION

Inductive power transfer (IPT) based on magnetic resonance coupling is widely used to supply energy cordlessly for electrical vehicles or trains [1]–[4], medical devices [5], [6], and other electronics [7], [8]. As to high power applications, such as wireless charging for electrical vehicles, the soft-switching is necessary for inverters at a relatively high operating frequency (i.e., 85 kHz). For a typical series-series (S-S) compensation IPT system, the inverter output voltage is squared wave while the current is sinusoid. When the current lags behind the voltage, the zero-voltage-switching (ZVS) condition is meet.

The simplest way to realize ZVS is to adjust the frequency of the switch so that the equivalent load of the inverter is weak inductive, that is to say, the equivalent impedance angle (the angle of inverter current lagging behind voltage, or ZVS angle) of the inverter is slightly larger than zero [9]. In a practical inductive power transfer system, the load of the receiver is usually a battery pack. The charging voltage and current of batteries change with the charging progress, resulting in the change of equivalent load at the receiving side and the inverter ZVS angle at the sending side. If the impedance angle is too large, the output power will be reduced. But a small or even less than zero impedance angle leads to the increase of loss and sharp temperature raising resulting by the switch operating in non-ZVS state. Therefore, it is necessary to design a controller to automatically adjust the impedance angle at a certain range. Reference [10] details how to implement an accurate ZVS control with a current hysteresis comparator and an enhanced phase detection methodology. However, the setting time reported by the literature is nearly 200 ms, which is too long considering the possible temperature rising and resulting device damage due to loss of ZVS under larger current. The unsatisfactory dynamics can be attributed to ZVS controller design without careful modeling and performance analysis.

Hence, it is necessary to model and analyze the IPT system in order to design a controller with better dynamical performances. Many modeling methods have been proposed for IPT

The associate editor coordinating the review of this manuscript and approving it for publication was Giambattista Gruosso.

systems. In [11] and [12], a nonlinear model for IPT using coupled mode theory is proposed. The coupled mode theory employees two variables, namely, the energy-amplitude and phase instead of current and voltage to describe dynamics of the system [13]. However, the concern of coupled mode is same complex to understand. Additionally, the phase variable θ of coupled mode hasn't relation with the ZVS angle and couldn't be used to analyze the ZVS condition directly. Small signal modeling method is commonly employed to establish the mathematical model for IPT system [14]–[17]. Reference [14] proposes a method to analyze high-order circuits by using the extended function description technology and the balance model reduction method. A two-loop control method and its modeling are proposed in [15] to eliminate the extra chopper stage at the receiving side. Issues of modeling and control of a multiphase phase-controlled inverter supplying the IPT are discussed in [16]. Reference [17] adopts an equivalent small parameter method (ESPM) to solve the proposed six-order nonlinear model, and symbolic-form steady-state periodic solutions are yielded.

Besides controlling the output voltage and current of the system discussed by above literatures, the modeling and control for ZVS angle is another focused issue. Reference [10] presents inverter ZVS control for IPT system, but mainly focuses on how to enhance the accuracy of the ZVS angle detection instead of ZVS modeling. Modeling and control methods regarding constant voltage/current and ZVS are discussed in [18] where the decoupling problem is mainly discussed. Reference [19] proposes a control strategy for efficiency optimization and ZVS of inverter at both sides for bidirectional IPT system, but lacks of the detail analysis for the controller performance.

To investigate the dynamic characteristics and design a controller with proper performance, the paper develops a 4-order dynamic model based on four state variables, namely, the energy-amplitudes and phases at both sides instead of voltages and currents which are employed by most literatures. Especially, one of the state variables is the ZVS angle, which makes a straightforward real dynamic model regarding how the ZVS angle is affected by the frequency. Another contribution of the paper is that the variables of amplitudes and phases are derived from the simple energy point of view, which is easier to understand than that from the complex coupled mode theory.

The structure of the paper is organized as follows: Section II investigates how the operating frequency influence the inverter ZVS angle of the S-S compensated IPT system. ZVS modeling and controller design method are presented in Section III. By using small signal modeling method, the nonlinear model of the system is linearized near the operating point and the transfer function is obtained to analyze the dynamic performance of ZVS regulating. Finally, PI controller in discrete domain is designed to maintain the stability of ZVS angle of the inverter. In Section IV, an experimental prototype is built and the ZVS angle control performance is tested.

II. INVERTER ZVS ANGLE

As to class-D inverter employed by the IPT system, the ZVS can be obtained as long as the load of the inverter is inductive or the inverter output impedance angle (or the ZVS angle) is higher than 0. The inverter output impedance angle is analyzed following.

A. ANALYSIS OF THE INVERTER OUTPUT IMPEDANCE ANGLE

A typical S-S compensated IPT system is depicted in Fig. 1 where V_{I} is the input DC voltage source, C_{Bus} is the DC bus filter capacitor, Q_1 and Q_2 are switches forming the half bridge inverter, C_1, L_1, r_1 are resonant capacitor, inductor and equivalent series resistance at the sending side, C_2, L_2, r_2 are resonant capacitor, inductor and equivalent series resistance at the receiving side, M is the coupling inductance between two coils, v_1 is the inverter output voltage, i_1 and i_2 are currents through each loop, respectively. Because of the high impedance, harmonic components of voltages and currents are neglected. Additionally, DC components of the inverter output voltage does not generate current through loops because of the capacitor C_1. Hence, Only the fundamental components of output voltages and currents, namely v_1, i_1 and i_2 are considered following. Under the inverter duty cycle of 0.5, the fundamental component of the inverter output voltage and current can be respectively expressed by

$$v_1 = \frac{2V_{\mathrm{I}}\cos(\omega t)}{\pi} \tag{1}$$

$$i_1 = I_{\mathrm{m1}}\cos(\omega t - \theta_1) \tag{2a}$$

where I_{m1}, θ_1 are the amplitude current of the sending side loop and the inverter output impedance angle (i.e., ZVS angle). Note that the phase angle of v_1 is assumed to be the reference. Apparently, the ZVS angle θ_1 can be introduced into the dynamic model directly. Additionally, the voltage across the resonant capacitor C_1 is

$$v_{\mathrm{C1}} = V_{\mathrm{Cm1}}\sin(\omega t - \theta_1) \tag{2b}$$

where V_{Cm1} is the amplitude voltage.

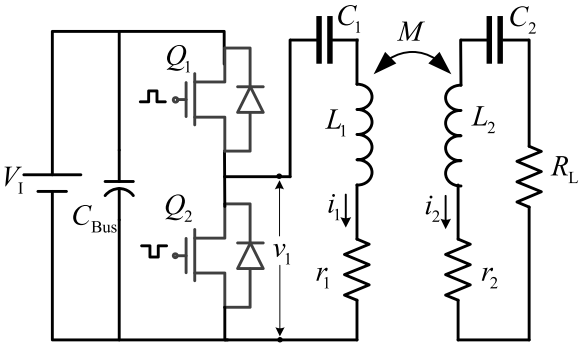

FIGURE 1. Schematic of S-S compensated IPT system driven by class-D half-bridge inverter.

TABLE 1. Parameters for impedance angle simulations.

Symbol	Prameter	Value
f	Operating frequency	60 kHz-100kHz
C_1, C_2	Resonant capacitances at both sides	117 nF
L_1, L_2	Resonant inductances at both sides	34 μH
r_1	Equivalent series resistances at sending side	80 mΩ
r_2	Equivalent series resistances at receiving side	40 mΩ
M	Coupling inductance	7.33 μH
R_L	Load resistance at the receiving side	4 Ω-50Ω
V_1	DC voltage	55 V
D	Inverter duty cycle	0.5

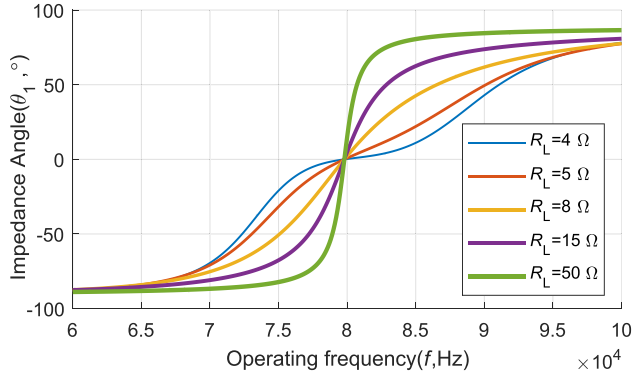

FIGURE 2. Inverter output impedance angle vs. operating frequency.

As to Fig. 1, one obtains the inverter output impedance angle by

$$\theta_1 = \arctan \frac{\text{imag}(\mathbf{Z})}{\text{real}(\mathbf{Z})} \tag{3}$$

where functions 'imag' and 'real' are employed to extract the imaginary and realistic parts, respectively, and the inverter output impedance $\mathbf{Z}$ is

$$\begin{aligned}\mathbf{Z} &= \mathbf{Z}_1 + \mathbf{Z}_{\text{ref}} = \mathbf{Z}_1 + \frac{(\omega M)^2}{\mathbf{Z}_2} \\ &= j\omega L_1 + \frac{1}{j\omega C_1} + r_1 + \frac{(\omega M)^2}{j\omega L_2 + \frac{1}{j\omega C_2} + r_2 + R_L}\end{aligned} \tag{4}$$

B. SIMULATION OF THE INVERTER OUTPUT IMPEDANCE ANGLE

To have a insight view of the impedance angle vs. the operating frequency and the load resistance, MATLAB simulations are conducted under parameters listed in Table. 1. Especially, the load resistance range is depended on the equivalent resistance of the battery pack. Take the battery pack employed by literature [21] as an example, its range is 3.5 Ω through 15.2 Ω with 9 batteries connected in series. Actually, for a battery pack with more batteries connected in series for a higher power level, its equivalent resistance increases correspondently. Hence, the load resistance range of 4 Ω through 50 Ω for the simulation is reasonable.

Fig. 2 shows that the invert output impedance phase angle θ_1 increases with the operating frequency f under given load resistance R_L. Hence, one can adjust the inverter impedance angle via regulating the operating frequency. Especially, an impedance angle weakly higher than 0 can be obtained via a properly adjusted operating frequency to maintain the inverter ZVS condition.

III. MODELING FOR ZVS ANGLE

A. DYNAMIC MODEL OF ZVS ANGLE

Based on the KVL, the dynamic functions of the system shown in Fig. 1 can be described by

$$\begin{cases} v_1 = i_1 r_1 + v_{C1} + L_1 \dfrac{\mathrm{d}i_1}{\mathrm{d}t} - M \dfrac{\mathrm{d}i_2}{\mathrm{d}t} \\ i_1 = C_1 \dfrac{\mathrm{d}v_{C1}}{\mathrm{d}t} \\ 0 = i_2(r_2 + R_L) + v_{C2} + L_2 \dfrac{\mathrm{d}i_2}{\mathrm{d}t} - M \dfrac{\mathrm{d}i_1}{\mathrm{d}t} \\ i_2 = C_2 \dfrac{\mathrm{d}v_{C2}}{\mathrm{d}t} \end{cases} \tag{5}$$

where v_{C1}, v_{C2} are the voltages across the resonant capacitor C_1 and C_2, respectively. Note that only the fundamental components of all currents and voltages are considered in (5).

Although (4) provides a dynamic model for the IPT system shown in Fig. 1, one can't get insight view on how the operating frequency influence the ZVS angle expressed by (2). Hence, part of variables in (4) (i.e., i_1, i_2, v_{C1} and v_{C2}) are expected to be replaced by ones directly involved in the ZVS angle θ_1. Following, energy amplitudes and phases are employed to model the dynamic model.

From the energy point of view, the energy a_1^2 stored in the sending resonant loop can be expressed by [20]

$$a_1^2 = \frac{1}{2} L_1 i_1^2 + \frac{1}{2} C_1 v_{C1}^2. \tag{6}$$

Because the energy of the sending loop is completed stored in the inductor L_1 when the current i_1 arrives at its amplitude, namely

$$a_1^2 = \frac{1}{2} L_1 \left(I_{m1} \cos(\omega t - \theta_1)\right)^2 \quad \text{under } \cos(\omega t - \theta_1) = 1, \tag{7}$$

one obtains

$$I_{m1} = \sqrt{\frac{2}{L_1}} a_1 \tag{8a}$$

With the same method, one obtains

$$V_{Cm1} = \sqrt{\frac{2}{C_1}} a_1 \tag{8b}$$

$$I_{m2} = \sqrt{\frac{2}{L_2}} a_2 \tag{8c}$$

$$V_{Cm2} = \sqrt{\frac{2}{C_2}} a_2 \tag{8d}$$

Substitution (8a) and (8b) into (2a) and (1) respectively yields

$$\begin{aligned} i_1 &= \sqrt{\frac{2}{L_1}} \times a_1 \cos(\omega t - \theta_1) \\ v_{C1} &= \sqrt{\frac{2}{C_1}} \times a_1 \sin(\omega t - \theta_1) \end{aligned} \tag{9a}$$

With the same method, the resonant current through L_2 and the voltage across C_2 are represented by

$$\begin{aligned} i_2 &= \sqrt{\frac{2}{L_2}} \times a_2 \cos(\omega t - \theta_2) \\ v_{C2} &= \sqrt{\frac{2}{C_2}} \times a_2 \sin(\omega t - \theta_2) \end{aligned} \tag{9b}$$

where θ_2 is the phase of the resonant current i_2 lagging behind the inducted voltage. Note that these newly introduced variables a_1, a_2, θ_1 and θ_2 vary slowly with time, namely, they nearly keep constant during one inverter switching cycle, while currents and voltages vary fast with time during one cycle.

The derivatives of the resonant currents and voltages depicted by (9) can be derived by

$$\begin{aligned} \frac{di_1}{dt} &= \sqrt{\frac{2}{L_1}} \cdot \left(\frac{da_1}{dt} \cos(\omega t - \theta_1) \right. \\ &\quad \left. - a_1 \sin(\omega t - \theta_1)(\omega - \frac{d\theta_1}{dt}) \right) \\ \frac{dv_{C1}}{dt} &= \sqrt{\frac{2}{C_1}} \cdot \left(\frac{da_1}{dt} \sin(\omega t - \theta_1) \right. \\ &\quad \left. + a_1 \cos(\omega t - \theta_1)(\omega - \frac{d\theta_1}{dt}) \right) \\ \frac{di_2}{dt} &= \sqrt{\frac{2}{L_2}} \cdot \left(\frac{da_2}{dt} \cos(\omega t - \theta_2) \right. \\ &\quad \left. - a_2 \sin(\omega t - \theta_2)(\omega - \frac{d\theta_2}{dt}) \right) \\ \frac{dv_{C2}}{dt} &= \sqrt{\frac{2}{C_2}} \cdot \left(\frac{da_2}{dt} \sin(\omega t - \theta_2) \right. \\ &\quad \left. + a_2 \cos(\omega t - \theta_2)(\omega - \frac{d\theta_2}{dt}) \right) \end{aligned} \tag{10}$$

Integration of (1), (5), (9) and (10) leads to a time-varying non-linear model with operating angular frequency ω as the input and energy-related variables a_1, a_2 and phases θ_1, θ_2 as outputs by

$$\begin{aligned} \frac{da_1}{dt} &= \cos(\omega t - \theta_1)[\omega_1 a_1 \sin(\omega t - \theta_1) \\ &\quad + \frac{1}{(L_1 L_2 - M^2)}(-\sqrt{\frac{L_1}{C_1}} \times L_2 a_1 \sin(\omega t - \theta_1) \\ &\quad - r_1 L_2 a_1 \cos(\omega t - \theta_1) - M\sqrt{\frac{L_1}{C_2}} \times a_2 \sin(\omega t - \theta_2) \\ &\quad - M\sqrt{\frac{L_1}{L_2}} \times (r_2 + R_L) a_2 \cos(\omega t - \theta_2) \\ &\quad + L_2 \frac{2V_I \cos(\omega t)}{\pi} \sqrt{\frac{L_1}{2}})] \end{aligned} \tag{11a}$$

$$\begin{aligned} \frac{d\theta_1}{dt} &= -\omega_1 \cos^2(\omega t - \theta_1) + \omega \\ &\quad - \frac{1}{(L_1 L_2 - M^2) a_1} \sin(\omega t - \theta_1) \\ &\quad \times [\sqrt{\frac{L_1}{C_1}} \times L_2 a_1 \sin(\omega t - \theta_1) + r_1 L_2 a_1 \cos(\omega t - \theta_1) \\ &\quad + M\sqrt{\frac{L_1}{C_2}} \times a_2 \sin(\omega t - \theta_2) \\ &\quad + M\sqrt{\frac{L_1}{L_2}} \times (r_2 + R_L) a_2 \cos(\omega t - \theta_2) \\ &\quad - \frac{2V_I L_2 \cos(\omega t)}{\pi} \sqrt{\frac{L_1}{2}}], \end{aligned} \tag{11b}$$

$$\begin{aligned} \frac{da_2}{dt} &= \cos(\omega t - \theta_2)[a_2 \omega_2 \sin(\omega t - \theta_2) \\ &\quad + \frac{1}{(L_1 L_2 - M^2)}(-M\sqrt{\frac{L_2}{C_1}} \times a_1 \sin(\omega t - \theta_1) \\ &\quad - M\sqrt{\frac{L_2}{L_1}} \times r_1 a_1 \cos(\omega t - \theta_1) \\ &\quad - L_1\sqrt{\frac{L_2}{C_2}} \times a_2 \sin(\omega t - \theta_2) \\ &\quad - L_1 (r_2 + R_L) a_2 \cos(\omega t - \theta_2) \\ &\quad + M \frac{2V_I \cos(\omega t)}{\pi} \sqrt{\frac{L_2}{2}})], \end{aligned} \tag{11c}$$

$$\begin{aligned} \frac{d\theta_2}{dt} &= -\omega_2 \cos^2(\omega t - \theta_1) + \omega - \frac{\sin(\omega t - \theta_2)}{(L_1 L_2 - M^2) a_2} \\ &\quad \times [M\sqrt{\frac{L_2}{C_1}} \times a_1 \sin(\omega t - \theta_1) \\ &\quad + M\sqrt{\frac{L_2}{L_1}} \times a_1 r_1 \cos(\omega t - \theta_1) \\ &\quad + L_1\sqrt{\frac{L_2}{C_2}} \times a_2 \sin(\omega t - \theta_2) \\ &\quad + L_1 (r_2 + R_L) a_2 \cos(\omega t - \theta_2) \\ &\quad - M\sqrt{\frac{L_2}{2}} \times \frac{2V_I \cos(\omega t)}{\pi}], \end{aligned} \tag{11d}$$

where ω_1 and ω_2 are the self-resonant angular frequency for each side depicted by

$$\begin{aligned} \omega_1 &= \frac{1}{\sqrt{L_1 C_1}} \\ \omega_2 &= \frac{1}{\sqrt{L_2 C_2}} \end{aligned} \tag{12}$$

B. LARGE-SIGNAL MODEL

The object of the paper is to investigate how the operating angular frequency ω affects the inverter ZVS angle θ_1 where both ω and θ_1 are slowly varying variables. Hence, one has to cancel the high-frequency time-variant terms depended on ωt such as $\cos(\omega t+\theta_1)$, $\sin(\omega t+\theta_1)$, $\cos(\omega t+\theta_2)$, $\sin(\omega t+\theta_2)$, and so on, while remains the expected low-frequency components related to ω and θ_1. Taking the average values of both sides of (11), one obtains the time-invariant averaged model depicted by

$$\begin{aligned}\frac{d\bar{a}_1}{dt} &= \frac{1}{L_1L_2-M^2}[-\frac{r_1L_2\bar{a}_1}{2}-M\sqrt{\frac{L_1}{C_2}}\times\frac{\bar{a}_2\sin(\bar{\theta}_1-\bar{\theta}_2)}{2}\\ &\quad -M\sqrt{\frac{L_1}{L_2}}\times\frac{(r_1+R_L)\bar{a}_2\cos(\bar{\theta}_1-\bar{\theta}_2)}{2}\\ &\quad +\sqrt{\frac{L_1}{2}}\frac{V_IL_2\cos\bar{\theta}_1}{\pi}] \qquad (13a)\\ \frac{d\bar{\theta}_1}{dt} &= \omega-\frac{\omega_1}{2}-\frac{1}{(L_1L_2-M^2)\bar{a}_1}[\\ &\quad \frac{L_2\bar{a}_1}{2}\sqrt{\frac{L_1}{C_1}}+M\sqrt{\frac{L_1}{C_2}}\times\frac{\bar{a}_2\cos(\bar{\theta}_1-\bar{\theta}_2)}{2}\\ &\quad -M\sqrt{\frac{L_1}{L_2}}\times\frac{(r_2+R_L)\bar{a}_2\sin(\bar{\theta}_1-\bar{\theta}_2)}{2}\\ &\quad +\sqrt{\frac{L_1}{2}}\times\frac{V_IL_2\sin\bar{\theta}_1}{\pi}] \qquad (13b)\\ \frac{d\bar{a}_2}{dt} &= \frac{1}{(L_1L_2-M^2)}(M\sqrt{\frac{L_2}{C_1}}\times\frac{\bar{a}_1\sin(\bar{\theta}_1-\bar{\theta}_2)}{2}\\ &\quad -M\sqrt{\frac{L_2}{L_1}}\times\frac{r_1\bar{a}_1\cos(\bar{\theta}_1-\bar{\theta}_2)}{2}\\ &\quad -\frac{L_1(r_2+R_L)\bar{a}_2}{2}+\sqrt{\frac{L_2}{2}}\times\frac{MV_I\cos\bar{\theta}_2}{\pi}) \qquad (13c)\\ \frac{d\bar{\theta}_2}{dt} &= \omega-\frac{\omega_2}{2}-\frac{1}{(L_1L_2-M^2)\bar{a}_2}\\ &\quad [\sqrt{\frac{L_2}{C_2}}\times\frac{L_1\bar{a}_2}{2}+M\sqrt{\frac{L_2}{C_1}}\times\frac{\bar{a}_1\cos(\bar{\theta}_1-\bar{\theta}_2)}{2}\\ &\quad +M\sqrt{\frac{L_2}{L_1}}\times\frac{r_1\bar{a}_1\sin(\bar{\theta}_1-\bar{\theta}_2)}{2}\\ &\quad +\frac{MV_I}{\pi}\sqrt{\frac{L_2}{2}}\times\sin(\bar{\theta}_2)] \qquad (13d)\end{aligned}$$

where $\bar{a}_1$ is the average of a_1 during one inverter switching cycle, and the same with $\bar{a}_2$, $\bar{\theta}_1$ and $\bar{\theta}_2$.The model represented by (13) is also known as the large-signal model which eliminates the high-frequency terms while remains low-frequency characteristics. The model depicts the envelope of the variables a_1, a_2 and phases θ_1, θ_2 in the converter under both steady-state and transient conditions.

C. LINEARIZED SMALL-SIGNAL MODEL

The large-signal model depicted by (13) contains both the steady state operating point and the small-signal model. The steady state solution can be extracted either by setting the large-signal differential equations to zeros or by using the fundamental harmonic analysis [11]. Based on the fundamental harmonic analysis expressed by (3) and (4), one obtains the inverter output impedance under parameters listed in Tab. 1 except $f = 82.5$ kHz and $R_{\rm L} = 8\ \Omega$ as $\mathbf{Z}_0 = 1.8405 + j0.8871\ \Omega$ and phase at the sending side $\theta_{10} = 0.449$. Herein, the steady state solution are represented by a_{10}, θ_{10}, a_{20} and θ_{20} for $\bar{a}_1$, $\bar{\theta}_1$, $\bar{a}_2$ and $\bar{\theta}_2$, respectively. The amplitude currents at the sending side and receiving side are $I_{\rm m1} = |v_1/\mathbf{Z}_0| = 15.58$ A and $I_{\rm m2} = |j\omega MI_{\rm m1}/\mathbf{Z}_{20}| = 7.29$ A, respectively. Based on (8a), one can obtain that $a_{10} = 0.071$. With the same method, θ_{20} anda_{20} are 0.140 and 0.033, respectively. As a result, the variable $\boldsymbol{x}$ consisting of $\bar{a}_1, \bar{\theta}_1, \bar{a}_2$ and $\bar{\theta}_2$ can be expressed by the steady state $\boldsymbol{x}_0$ plus the small perturbation $\hat{\boldsymbol{x}}$ by

$$\boldsymbol{x} = \boldsymbol{x}_0 + \hat{\boldsymbol{x}} \qquad (14)$$

where $\boldsymbol{x}_0 = [a_{10}\ \theta_{10}\ a_{20}\ \theta_{20}]^{\rm T}$ and $\hat{\boldsymbol{x}} = [\hat{a}_1\ \ \hat{\theta}_1\ \ \hat{a}_2\ \ \hat{\theta}_2]^T$.

Substituting (14) into (13), extending each variable-involved term around its steady state solution using Taylor's series and remaining the linearized terms while discarding the high-order terms lead to the small-signal state space model in matrix form as

$$\begin{aligned}\frac{d\hat{\boldsymbol{x}}}{dt} &= \mathbf{A}\cdot\hat{\boldsymbol{x}}+\mathbf{B}\cdot\hat{\boldsymbol{u}}\\ \hat{\boldsymbol{y}} &= \mathbf{C}\cdot\hat{\boldsymbol{x}},\end{aligned} \qquad (15)$$

where $\hat{u} = f$ and $\hat{y} = \frac{180}{\pi}\hat{\theta}_1$ are the input and output of the model, respectively. Matrix **A**, **B** and **C** are as shown in (16a)–(16c) at the bottom of the next page, where

$$\begin{aligned}k_0 &= L_1L_2-M^2, \quad k_1 = \frac{M}{2}\sqrt{\frac{L_1}{C_2}},\\ k_2 &= \frac{M}{2}\sqrt{\frac{L_1}{L_2}}\times(r_2+R_L), \quad k_3 = L_2\sqrt{\frac{L_1}{2}}\times\frac{V_I}{\pi},\\ k_4 &= \frac{Mr_1}{2}\sqrt{\frac{L_2}{L_1}}, \quad k_5 = M\sqrt{\frac{L_2}{2}}\times\frac{V_I}{\pi},\\ k_6 &= \frac{M}{2}\sqrt{\frac{L_2}{C_1}}, \quad \Delta_0 = \theta_{10}-\theta_{20}\end{aligned} \qquad (16d)$$

Substitution $a_{10}, \theta_{10}, a_{20}, \theta_{20}$ and parameters listed in Tab. 1 except $f = 82.5$ kHz and $R_{\rm L} = 8\ \Omega$ into (15a) yields

$$\mathbf{A} = \begin{bmatrix} -1200 & -2500 & -42700 & 1500\\ 497400 & -8400 & -649200 & -20000\\ 17000 & 3800 & -124000 & -3900\\ -1635600 & 36300 & 3556800 & -21900\end{bmatrix} \qquad (17)$$

D. CONTROLLER DESIGN

The open-loop transfer function of model (14) can be obtained with MATLAB

$$G(s) = \frac{y(s)}{u(s)} = \frac{360s^3 + 4.584e^7 s^2 + 7.45e^{12}s + 2.394e^{17}}{s^4 + 1.556e^5 s^3 + 2.558e^{10}s^2 + 1.301e^{15}s + 1.906e^{19}} \tag{18}$$

For the practical application of the IPT system, the model needs to be discretized to design a digital controller. The measurement should be conducted after the resonant current keeps relatively stable with each frequency change. Hence, a sampling frequency of 4 kHz (i.e., the sampling time $T_S = 2.5e^{-4}$ s) is employed. Namely, the measurement is executed after about 20 switching cycles for the IPT system with a typical operating frequency of 85 kHz. The discretized model of (18) under 4 kHz sampling frequency is obtained with MATLAB under zero-order-hold by

$$G_r(z) = \frac{y(z)}{u(z)} = \frac{1.255e^{-2}z^3 - 3.72e^{-7}z^2 + 1.152e^{-11}z - 2.207e^{-16}}{z^4 - 1.189e^{-3}z^3 + 1.143e^{-7}z^2 - 1.688e^{-12}z + 1.289e^{-17}} \tag{19}$$

To control the IPT system for a prefer ZVS angle, a PI controller in discrete time is designed by

$$P(z) = K_P\left(1 + \frac{T_S}{T_I}\frac{z}{z-1}\right) \tag{20}$$

The proportional an integral parameter of (20) are K_P and $K_I = K_P T_S/T_I$ where T_I is the integral time. After some MATLAB simulation of unit-step response for the feedback system with the designed PI controller, a set of PI parameters are selected by $K_p = 42$ and $T_I = 2 \times 10^{-3}$(i.e., $K_I = 5.25$). The stability phase and margin characteristics of the model with the designed controller is depicted in Fig. 3(a). One can see from the phase and amplitude margin that the control-loop is stable. It can be calculated by MATLAB that the amplitude margin is 5.05dB and the phase margin is 120°, which shows the robustness of the system with PI controller. The unit-step response is depicted in Fig. 3(b). One can see that the setting time of the controller is about 20 ms. Additionally, there is a fluctuation at the first step of the response. This is because the P parameter of the PI controller is relatively high ($K_P = 42$), the zero-state response of the first step output from the PI controller is some high, which shows a sharp increase. After this sharp increase, the PI controller drops the output to a relatively low value.

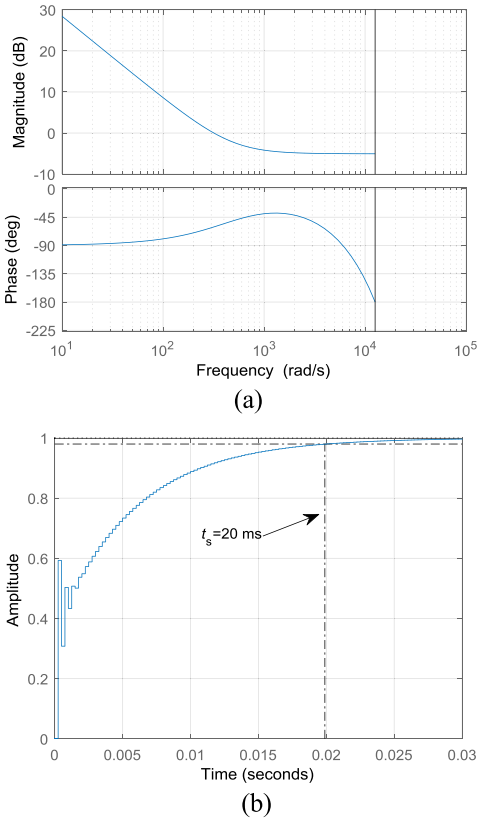

FIGURE 3. Performances of the system with PI controller with (a) the stability phase and margin characteristics and (b) Unity step response of the close-loop system.

IV. PROTOTYPE AND EXPERIMENTAL VERIFICATION

A. PROTOTYPE DESIGN

A series-series compensated IPT prototype shown in Fig. 4 is built to verify of the model and controller performance. The prototype is composed of a DC source, an inverter, resonant capacitor banks, resonant coils, a rectifier at the receiving side and a load resistance bank. The output voltage of the DC source can be regulated by hand.

$$\mathbf{A} = \frac{1}{k_0}\begin{bmatrix} \frac{-r_1 L_2}{2} & -k_1 a_{20}\cos\Delta_0 + k_2 a_{20}\sin\Delta_0 - k_3\sin\theta_{10} & -k_1\sin\Delta_0 - k_2\cos\Delta_0 & k_1 a_{20}\cos\Delta_0 - k_2 a_{20}\sin\Delta_0 \\ -\frac{k_1 a_{20}\cos\Delta_0 - k_2 a_{20}\sin\Delta_0 + k_2\sin\theta_{10}}{a_{10}^2} & \frac{-k_1 a_{20}\sin\Delta_0 - k_2 a_{20}\cos\Delta + k_3\cos\theta_{10}}{a_1} & \frac{k_1\cos\Delta_0 - k_2\sin\Delta_0}{a_{10}} & \frac{k_1 a_{20}\sin\Delta_0 + k_2 a_{20}\cos\Delta_0}{a_{10}} \\ \frac{k_6\sin\Delta_0 - k_4\cos\Delta_0}{a_{20}} & \frac{k_6 a_{10}\cos\Delta_0 + k_4 a_{10}\sin\Delta_0}{a_{20}} & -\frac{(r_2+R_L)L_1}{2} & -\frac{k_6 a_{20}\cos\Delta_0 - k_4 a_{10}\sin\Delta_0 - k_5\sin\theta_{20}}{a_{10}} \\ \frac{k_6\cos\Delta_0 + k_4\sin\Delta_0}{a_{20}} & \frac{-k_6 a_{10}\sin\Delta_0 + k_4 a_{10}\cos\Delta_0}{a_{20}} & -\frac{k_6 a_{10}\cos\Delta_0 + k_4^2 a_{10}\sin\Delta_0 + k_5\sin\theta_{20}}{a_{20}^2} & \frac{k_6 a_{10}\sin\Delta_0 - k_4 a_{10}\cos\Delta_0 - k_5\cos\theta_{20}}{a_{20}} \end{bmatrix}, \tag{16a}$$

$$\mathbf{B} = [0 \quad 2\pi \quad 0 \quad 2\pi]^T, \tag{16b}$$

$$\mathbf{C} = [0 \quad 57.30 \quad 0 \quad 0]^T \tag{16c}$$

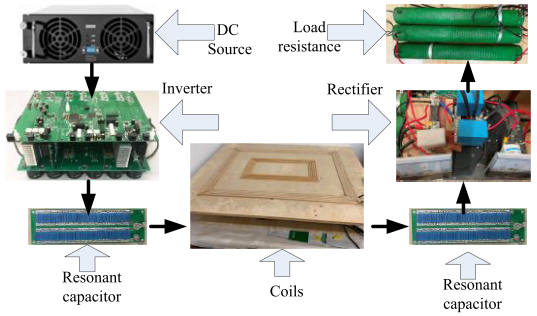

FIGURE 4. Prototype of the S-S compensated IPT system.

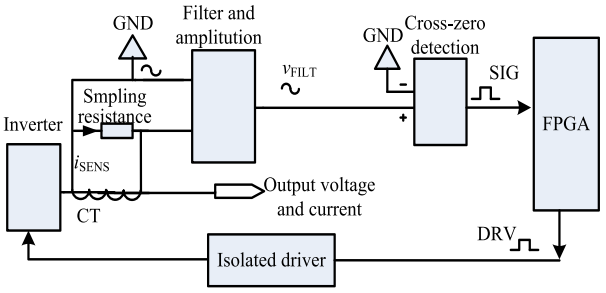

FIGURE 5. Detecting circuit of ZVS angle.

For the half-bridge inverter, its power stage is mainly built by two MOSFETs of IPW65R041CFD. The controller is implemented by an ARM of STM322F407VGT and a FPGA of XC6SLX9-3TQG1441. The controller code is operating in the ARM which measures the ZVS angle, calculates the output switch frequency, and sends the corresponding clock count to the FPGA according to the frequency. The FPGA provides driver signals for MOSFETs according to the clock count. For the FPGA with a clock frequency of 199.54MHz, the clock count is calculated by the clock frequency divided by the switch frequency. For example, a 2418 CLKs of clock count means a switch frequency of 82.5 kHz, namely, the state of the inverter switches is changed every 1209 FPGA CLKs.

Coils with a gap of 20 cm and 4 turns at both sides are the same, namely, 90 cm × 70 cm for the outer width and 87 cm × 67 cm for the inner width. The coil is wound by Litz wire of 2000 isolated strands with a diameter of 0.1 mm for each strand. The full bride rectifier at the receiving side employees 2 rectifier module of VS-UFB280FA40.

A phase angle measurement between the inverter output current and voltage is needed to implement the described control. Hence, a phase detecting circuit depicted by Fig. 5 is designed. With a 1:50 current transducer (i.e., CT), the inverter current is transferred to a low amplitude one (i.e., i_{SENS}) which passes through a sampling resistance of 1 Ω. After filtering, amplification and cross-zero detection, the AC voltage across the sampling resistance is transferred into a squared signal SIG and sent to the FPGA. The operational amplifier and cross-zero detecting employed in the circuit are LM7171 and TS3011, respectively. The phase of the output voltage fundamental component can be represented by that of the driver signal of the inverter upper switch approximately if the dead time and the driver signal transmission delay are ignored. Hence, the ZVS angle is obtained by the FPGA via comparing the phases between SIG and DRV. The driver signal DRV is generated by FPGA. Additionally, the detected ZVS angle is stored by the ARM per 1 ms and can be uploaded to the private computer via ARM's UART module and RS232 communication cable when required.

The process of the wireless charging for electrical vehicle can be divided into three stages, namely, the constant current one, the constant voltage one and the trickle one. With the progress of the charging, the equivalent load resistance (the charging voltage divided by the current) of the battery pack is increasing. Hence, two experiments for the sharp raise of the load resistance where the resistance changes from 5 Ω to 10 Ω and 10 Ω to 15 Ω were conducted. Additionally, another experiment for the stage of charging start is conducted where the controller begins to work when the input DC voltage of the inverter arrives at 55 V. In practice, the load resistance consists of some power resistance of 10 Ω connected in parallel or series while the sharp resistance change is simulated via the opening or closing of an air switch.

For the digital controller, a position control algorithm expressed by

$$f(k+1) = K_p \times E_{rr}(k) + K_I \times \sum (E_{rr}(k)) \qquad (21)$$

is developed in the ARM, where $E_{rr}(k)$ represents the phase deviation of the k^{th} calculation and $\sum(E_{rr}(k))$ represents the accumulation of it till the k^{th}, respectively. PI parameters are the same with those for Fig. 3, namely, $K_{\mathrm{p}} = 42$ and $K_{\mathrm{I}} = 5.25$, respectively.

B. EXPERIMENT OF ZVS CONTROLL FOR THE CHARGING START-UP

The output from the TS3011 is not stable when the current of the inverter is relatively low (namely, the input DC source is low). Hence, the controller begins to execute only under the input DC voltage is above 55 V while stops below 55 V. Fig. 6 depicts the regulating process for the start-up of the system under the load resistance of 10 Ω, the reference ZVS angle of 30°, the beginning operating frequency of 81 kHz, the initial ZVS angle of 13.7°, and other parameters listed in Tab. 1. For the oscilloscope, the channel 1, 2 and 3 measure the half-bridge inverter output voltage (namely, the Drain-Source voltage of the inverter lower switch), the driver signal of the inverter upper switch and the inverter output current, respectively. Fig. 6(a) depicts the original waves of the inverter output voltage and current when the ZVS controller doesn't work under an input DC voltage of 50 V, the operating frequency of 81 kHz and a detected ZVS angle about 13.7°. Theoretically, the inverter switch operates at the ZVS condition under a ZVS angle of 13.7°. However, the detected 13.7° is not the real angle that the current lags behind the voltage of the inverter because of the transition delay of the driver signal

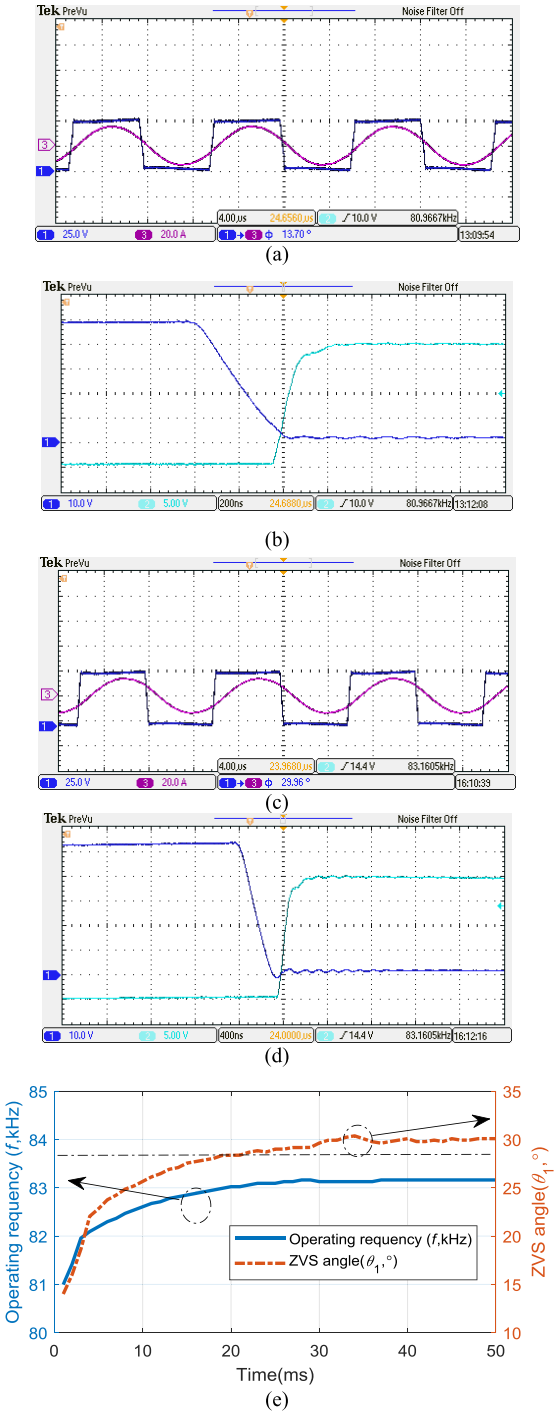

FIGURE 6. ZVS control experiment for the charging start-up.

and the dead time. The scene can be depicted by Fig. 6(b) where a small area of overlap exists when both the switch Drain-Source voltage and the switch turn-on driver signal are above 0. That's to say, the switch is turned on when the Drain-Source voltage is not zero, namely, the switch losses the ZVS condition. Hence, a slightly higher detected ZVS angle above than 13.7° is required to obtain a ZVS state. As a result, a reference of 30° is employed for the ZVS controller to trace.

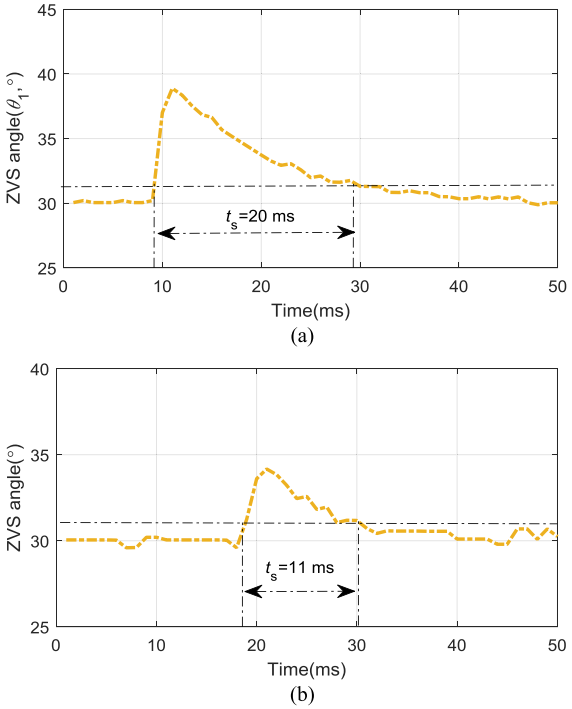

FIGURE 7. ZVS control experiment for the load change.

When the inverter input voltage (i.e., DC source voltage) is increased a value slightly higher than 55 V, the ZVS controller begins to operate to trace the reference angle of 30°. Fig. 6(c) shows the regulation result for the waves of the inverter output voltage and current with the ZVS controller. Fig. 6(d) depicts the waves both the switch Drain-Source voltage and the driver signal of switch turn-on under 30° ZVS angle where no overlap between them is observed. Namely, the inverter operates at ZVS condition under the frequency output by the ZVS controller. With the data of the angle and frequency extracted from the ARM, one plots the regulating process of the charging start-up regarding to the ZVS angle and the operating frequency in Fig. 6(e). The data are uploaded from the ARM to the private computer via RS232 cable. It can be seen that the setting time is about 20 ms, which is almost equal to the simulated one by Fig. 3(a).

C. EXPERIMENT OF ZVS CONTROL FOR LOAD CHANGE

The sharp change of the load resistance can be implemented by removing one of the parallel resistances via opening the air switch. For example, a load resistance change of 5 Ω to 10 Ω can be obtained by removing one of 10 Ω resistances from two 10 Ω resistances connected in parallel and the same with 10 Ω to 15 Ω. The regulating process of the ZVS angle is depicted by Fig. 7, where (a) is for the load change of 5 Ω to 10 Ω and (b) for 10 Ω to 15 Ω. The experiments were conducted under 56 V input DC voltage for the inverter where the original ZVS angle are both 30°. The setting time are about 20 ms and 11 ms for various cases, respectively. The phase angle data are uploaded from the ARM via RS232 cable.

V. CONCLUSION

Based on the expressions of energy amplitude and phase, an 4-order state space model of the inverter ZVS angle is obtained and linearized via small-signal modeling method for the S-S compensated IPT system. Based on the obtained model, a PI controller is designed and the controller parameters are optimized according to the dynamics. Experiments verify that the controller maintains the ZVS condition via regulating the operating frequency based on the difference of the detected inverter ZVS angle and the reference one.

In spite of various setting times depicted in Fig. (6) and (7) under various application cases with different system parameters, they are closed to the simulated one shown in Fig. 3 (i.e., 16 ms). The differences are mainly due to the deviation of the operating points from the designed one in terms of the operating frequency as well as the load resistance. Regarding the resistance, the load resistance for the modeling and simulation is $R_{\mathrm{L}} = 8\ \Omega$ while a change from 5 Ω to 10 Ω and 5 Ω to 10 Ω for the experiments shown in Fig. 7, respectively. Additionally, the transmit delay of the switch driver signal and the dead time of the inverter also affect the practical regulating process of ZVS angle.

Experiments show that the controller trances the reference within short times (i.e., about 20 ms) under various cases, which verifies that the modeling and designed controller are reasonable to maintain the inverter ZVS condition. The designed controller has good dynamics even the operation point deviating from the designed one to certain extends, which shows a nice robustness regarding to the ZVS angle of the IPT system.

REFERENCES

[1] Q. Deng, J. Liu, D. Czarkowski, W. Hu, and H. Zhou, "An inductive power transfer system supplied by a multiphase parallel inverter," *IEEE Trans. Ind. Electron.*, vol. 64, no. 9, pp. 7039–7048, Sep. 2017.

[2] J. Tian and A. P. Hu, "A DC-voltage-controlled variable capacitor for stabilizing the ZVS frequency of a resonant converter for wireless power transfer," *IEEE Trans. Power Electron.*, vol. 32, no. 3, pp. 2312–2318, Mar. 2016.

[3] Q. Deng, P. Sun, W. Hu, D. Czarkowski, M. K. Kazimierczuk, and H. Zhou, "Modular parallel multi-inverter system for high-power inductive power transfer," *IEEE Trans. Power Electron.*, vol. 34, no. 10, pp. 9422–9434, Oct. 2019.

[4] J. H. Kim, B.-S. Lee, J.-H. Lee, S.-H. Lee, C.-B. Park, S.-M. Jung, S.-G. Lee, K.-P. Yi, and J. Baek, "Development of 1-MW inductive power transfer system for a high-speed train," *IEEE Trans. Ind. Electron.*, vol. 62, no. 10, pp. 6242–6250, Oct. 2015.

[5] B. Lee, M. Kiani, and M. Ghovanloo, "A triple-loop inductive power transmission system for biomedical applications," *IEEE Trans. Biomed. Circuits Syst.*, vol. 10, no. 1, pp. 138–148, Feb. 2016.

[6] B. J. Delong, A. Kiourti, and J. L. Volakis, "A radiating near-field patch rectenna for wireless power transfer to medical implants at 2.4 GHz," *IEEE J. Electromagn., RF, Microw. Med. Biol.*, vol. 2, no. 1, pp. 64–69, Mar. 2018.

[7] J. Park, D. Kim, K. Hwang, H. H. Park, S. I. Kwak, J. H. Kwon, and S. Ahn, "A resonant reactive shielding for planar wireless power transfer system in smartphone application," *IEEE Trans. Electromagn. Compat.*, vol. 59, no. 2, pp. 695–703, Apr. 2017.

[8] Z. Ai, Y. Liu, F. Song, and H. Zhang, "A smart collaborative charging algorithm for mobile power distribution in 5G networks," *IEEE Access*, vol. 6, pp. 28668–28679, 2018.

[9] M. K. Kazimierczuk and D. Czarkowski, "Class D series-resonant inverter," in *Resonant Power Converters*, 2nd ed. Hoboken, NJ, USA: Wiley, 2011, ch. 6, pp. 143–191.

[10] Y. Jiang, L. Wang, Y. Wang, J. Liu, X. Li, and G. Ning, "Analysis, design, and implementation of accurate ZVS angle control for EV battery charging in wireless high-power transfer," *IEEE Trans. Ind. Electron.*, vol. 66, no. 5, pp. 4075–4085, May 2019.

[11] H. Li, K. Wang, L. Huang, W. Chen, and X. Yang, "Dynamic modeling based on coupled modes for wireless power transfer systems," *IEEE Trans. Power Electron.*, vol. 30, no. 11, pp. 6245–6253, Nov. 2015.

[12] H. Li, J. Li, L. Huang, K. Wang, and X. Yang, "A novel dynamic modeling method for wireless power transfer systems," in *Proc. IEEE Appl. Power Electron. Conf. Expo.*, Mar. 2015, pp. 2740–2743.

[13] A. Kurs, A. Karalis, R. Moffatt, J. D. Joannopoulos, P. Fisher, and M. Soljačić, "Wireless power transfer via strongly coupled magnetic resonances," *Science*, vol. 317, no. 5834, pp. 83–86, 2007.

[14] Z. U. Zahid, Z. M. Dalala, C. Zheng, R. Chen, W. E. Faraci, J.-S. J. Lai, G. Lisi, and D. Anderson, "Modeling and control of series–series compensated inductive power transfer system," *IEEE J. Emerg. Sel. Topics Power Electron.*, vol. 3, no. 1, pp. 111–123, Mar. 2015.

[15] S. Samanta and A. K. Rathore, "Small-signal modeling and closed-loop control of a parallel–series/series resonant converter for wireless inductive power transfer," *IEEE Trans. Ind. Electron.*, vol. 66, no. 1, pp. 172–182, Jan. 2019.

[16] Q. Deng, Z. Wang, C. Chen, D. Czarkowski, M. K. Kazimierczuk, H. Zhou, and W. Hu, "Modeling and control of inductive power transfer system supplied by multiphase phase-controlled inverter," *IEEE Trans. Power Electron.*, vol. 34, no. 9, pp. 9303–9315, Sep. 2019.

[17] Y. Chen, W. Xiao, Z. Guan, B. Zhang, D. Qiu, and M. Wu, "Nonlinear modeling and harmonic analysis of magnetic resonant WPT system based on equivalent small parameter method," *IEEE Trans. Ind. Electron.*, vol. 66, no. 8, pp. 6604–6612, Aug. 2019.

[18] C. Chen, H. Zhou, Q. Deng, W. Hu, Y. Yu, X. Lu, and J. Lai, "Modeling and decoupled control of inductive power transfer to implement constant current/voltage charging and ZVS operating for electric vehicles," *IEEE Access*, vol. 6, pp. 59917–59928, 2018.

[19] X. Zhang, T. Cai, S. Duan, H. Feng, H. Hu, J. Niu, and C. Chen, "A control strategy for efficiency optimization and wide ZVS operation range in bidirectional inductive power transfer system," *IEEE Trans. Ind. Electron.*, vol. 66, no. 8, pp. 5958–5969, Aug. 2019.

[20] M. K. Kazimierczuk and D. Czarkowski, "Class D series resonant inverters," in *Resonant Power Converters*, 2nd ed. Hoboken, NJ, USA: Wiley, 2011, ch. 6.

[21] Q. Deng, J. Liu, D. Czarkowski, M. Bojarski, E. Asa, and F. de Leon, "Design of a wireless charging system with a phase-controlled inverter under varying parameters," *IET Power Electron.*, vol. 9, no. 13, pp. 2461–2470, Oct. 2016.

JIANGTAO LIU received the B.S. and M.Sc. degrees in control theory and applications and the Ph.D. degree in electrical engineering from Wuhan University, Wuhan, China, in 2003, 2010, and 2013, respectively.

In June 2003, she joined the School of Physical, Mechanical and Electrical Engineering, Hubei University of Education, Wuhan, where she is currently an Associate Professor. From 2013 to 2014, she was a Visiting Scholar with the New York University Tandon School of Engineering. She was a Visiting Scholar with Wuhan University, from 2017 to 2018. Her research interests include wireless power transfer and noise reduction for power transformers.

QIJUN DENG was born in Wuhan, China, in 1975. He received the B.S. and M.Sc. degrees in mechanical engineering and the Ph.D. degree in computer application technology from Wuhan University, Wuhan, China, in 1999, 2002, and 2005, respectively. In June 2005, he joined the Department of Automation (which now is merged into School of Electrical Engineering and Automation), Wuhan University, where he is currently a Professor. From 2013 to 2014, he was a Visiting Scholar with the New York University Tandon School of Engineering. His research interests include wireless power transfer, distribution automation, and electrical power informatics.

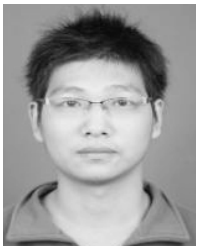

WENBIN WANG received the B.S. degree from the Wenhua College, Huazhong University of Science and Technology, Wuhan, China. in 2008, and the M.Sc. degree from the Wuhan University of Technology, Wuhan, in 2011. He is currently the Head of the New Energy and Microgrid Technology Department, Distribution Network Technology Center, State Grid Jiangxi Electric Power Research Institute, which is involved in distributed energy grid testing.

ZHIFAN LI was born in 1997. He received the B.S. degree in automation from Wuhan University, Wuhan, China, in 2019, where he is currently pursuing the M.Sc. degree with the School of Electrical Engineering and Automation. His current research interests include the areas of wireless power transfer and system identification.